The Astrophysical Journal, 954:98 (11pp), 2023 September 1 https://doi.org/10.3847/1538-4357/ace71f

Galaxy Quenching with Mass Growth History of Galaxy Groups and Clusters: The Importance of Post-processing

So-Myoung Park[1], Kyungwon Chun[1], Jihye Shin[1], Hyunjin Jeong[1], Joon Hyeop Lee[1], Mina Pak[1,2,3], Rory Smith[4], and Jae-Woo Kim[1]
[1] Korea Astronomy and Space Science Institute, 776 Daedeok-daero, Yuseong-gu, Daejeon 34055, Republic of Korea; kwchun@kasi.re.kr
[2] School of Mathematical and Physical Sciences, Macquarie University, Sydney, NSW 2109, Australia
[3] ARC Centre of Excellence for All Sky Astrophysics in 3 Dimensions (ASTRO 3D), Australia
[4] Universidad Técnica Federico Santa María, 3939 Vicuña Mackenna, San Joaquín, Santiago 8940897, Chile
Received 2023 March 26; revised 2023 July 3; accepted 2023 July 11; published 2023 August 25

Abstract

We investigate the fraction of quenched satellite galaxies in host galaxy groups and clusters using TNG300 in the IllustrisTNG cosmological magnetohydrodynamical simulations. The simulations show that most satellites are quenched after they fall into their final hosts, and that post-processing is a more dominant mechanism of galaxy quenching than pre-processing. We find that the fraction of quenched satellites at $z = 0$ increases with host mass, which implies that more massive hosts have higher quenching efficiency because they have more massive groups infalling. Furthermore, we find that hosts that have many early-infall satellites show a higher fraction of quenched satellites at $z = 0$ than those that have many late-infall satellites, which results in a scatter of the quenched fraction of satellites in a given mass range of hosts at $z = 0$. Our results highlight the significance of the mass of hosts and the different infall times of satellites in understanding galaxy quenching.

Unified Astronomy Thesaurus concepts: Galaxy quenching (2040); Galaxy evolution (594); Galaxy clusters (584); Galaxy groups (597); Red sequence galaxies (1373); Astronomical simulations (1857)

1. Introduction

Galaxies at low redshift are sorted into two populations by their star formation (SF) activity. One is disk-like "star-forming" galaxies that have ongoing SF, so young stellar populations with blue colors are observed. The other is elliptical-like "quenched (passive)" galaxies whose SF activity is strongly suppressed, so old stellar populations with red colors are observed. Galaxy quenching is closely related to various galaxy properties such as morphology, color, age, star formation rate (SFR), and kinematics (e.g., Kauffmann et al. 2003; Fang et al. 2013; Brownson et al. 2022, and references therein). Thus, understanding when, where, and how galaxies halt SF is one of the important topics in extragalactic astronomy.

In the observation, galaxies whose stellar mass is larger than $10^{10}\,M_{\odot}$ show low SFR (specific SFR $\leqslant 10^{-11}$ yr^{-1}) regardless of the environment, called "mass quenching" (e.g., Peng et al. 2010, 2012; Man & Belli 2018, and references therein). In this case, all of the internal processes of galaxies (secular evolution) that include outflows from stellar winds, supernova explosion, and active galactic nucleus (AGN) feedback decrease SFR (e.g., Di Matteo et al. 2005; Wake et al. 2012). On the other hand, in a high-density environment, the SFR of low-mass galaxies whose stellar mass is smaller than $10^{10}\,M_{\odot}$ is also suppressed, defined as "environmental quenching" (e.g., Jaffé et al. 2016; Crossett et al. 2017; Medling et al. 2018; Schaefer et al. 2019; González Delgado et al. 2022). In this case, there are various mechanisms that stop the SF of galaxies (for a recent review, see Cortese 2021): ram pressure stripping (Gunn & Gott 1972), tidal stripping (Merritt 1984), strangulation or starvation (Larson et al. 1980; Balogh et al. 2000), and harassment (Gallagher et al. 1972). These two quenching mechanisms have been consistently suggested to describe the observed properties of passive galaxies (e.g., Contini et al. 2020; Li et al. 2020).

In the framework of the Lambda cold dark matter (ΛCDM) model, it is widely accepted that galaxies are growing hierarchically, which means low-mass galaxies are the fundamental building blocks for cosmological structure formation. In this hierarchical paradigm, low-mass galaxies that fall into high-mass galaxies and/or the larger structures become their satellites, which are expected to be merged eventually. During their first orbital passage to the pericenter, the SF activities of satellites are highly suppressed by ram pressure and tidal stripping, called "post-processing" (e.g., Gabor et al. 2010; Vijayaraghavan & Ricker 2013; Donnari et al. 2021b). Interestingly, the SFR suppression of satellites is known to start even before the satellites fall into the larger structures, known as "pre-processing" (e.g., Fujita 2004; Hou et al. 2014; van der Burg et al. 2018; Sarron et al. 2019; Sarron & Conselice 2021; Mishra et al. 2023). Various simulations and observations have been used to study the quenching mechanism of galaxies (e.g., Bahé et al. 2013, 2019; Contini et al. 2020; Li et al. 2020; Rhee et al. 2020; Donnari et al. 2021b; Reeves et al. 2023, and references therein), but the relative amount of pre- and post-processing for galaxy quenching is still under discussion.

Since the galaxy groups and clusters are built up with satellites accreted from the outside, the fraction of quenched satellites can be a result that reflects both pre- and post-processing. In this paper, we use the IllustrisTNG simulation to investigate how the fraction of quenched satellites in galaxy groups and clusters is determined by the pre- and post-processing. We also examine the relationship between the

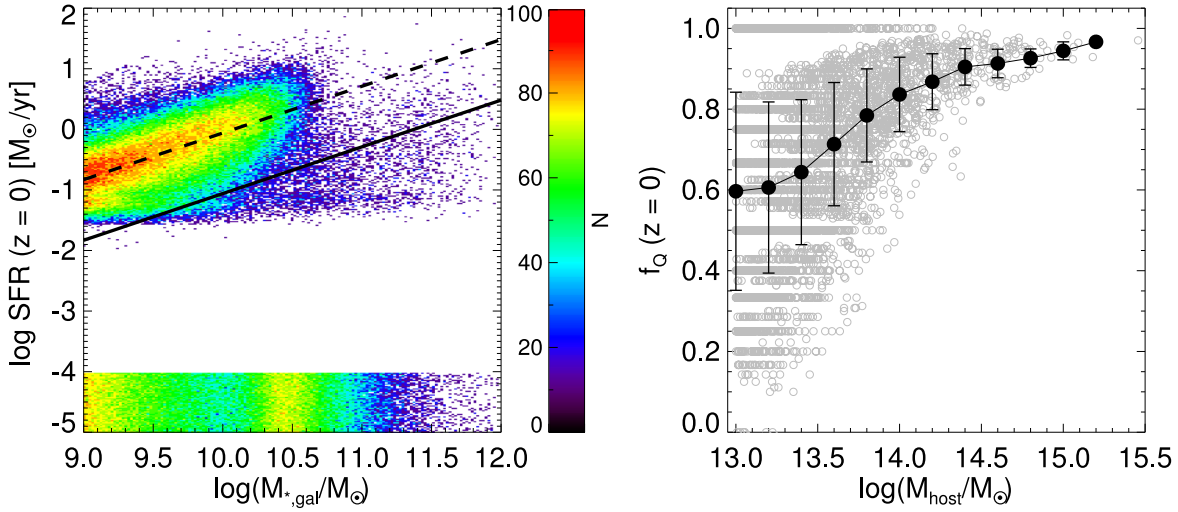

Figure 1. Left: SFR as a function of $M_{*,\mathrm{gal}}$. The black dashed and solid lines represent the star-forming MS and the line 1 dex below it, respectively. The color scale represents the number of galaxies in each pixel. We define the "quenched galaxy" whose SFR is 1 dex below the star-forming MS. Galaxies with a zero SFR value are randomly assigned a logarithmic SFR value between -5 and -4 solely to illustrate their existence. Right: number fraction of quenched galaxies out of all galaxies in individual groups and clusters (f_{Q}) as a function of M_{host} at $z = 0$. Black dots are the mean f_{Q} in each mass bin with an error bar indicating the standard deviation. In the range of low-mass hosts, there are points along the same value of $f_{\mathrm{Q}}(z = 0)$. These low-mass hosts have a small number of satellites (∼4.2 satellites on average), so there is a high probability that the value of $f_{\mathrm{Q}}(z = 0)$ is discrete.

fraction of quenched satellites at $z = 0$ and various properties of host groups and clusters.

This paper is organized as follows. In Section 2, we introduce the IllustrisTNG simulations and how we select sample galaxies in our study. In Section 3, we investigate whether pre- or post-processing is more dominant for galaxy quenching and what makes a diversity of the fraction of quenched galaxies at $z = 0$. Section 4 shows which properties of hosts are related to the quenched fractions, and the effect of the passage of the pericenter of hosts on quenching is examined in Section 5. Section 6 summarizes our results.

2. Method

2.1. The IllustrisTNG Simulations

To examine the quenched fraction of satellites in each galaxy group and cluster, we use the cosmological magnetohydrodynamical simulations of the IllustrisTNG project (hereafter IllustrisTNG),[5] which is composed of three different simulation volumes whose one side length is 50, 100, and 300 Mpc: TNG50, TNG100, and TNG300, respectively (Marinacci et al. 2018; Naiman et al. 2018; Nelson et al. 2018; Pillepich et al. 2018a; Springel et al. 2018; Nelson et al. 2019; Pillepich et al. 2019). To secure the best statistics for the galaxy groups and clusters, we use the TNG300 simulation, which has the largest volume of $(300\,\mathrm{Mpc})^3$. The initial mass resolutions of the dark matter (DM) particle and the gas cell are 5.0×10^7 and $1.1 \times 10^7\,M_\odot$, respectively. Detailed baryonic physics bringing the galaxy formation can be found in Weinberger et al. (2017) and Pillepich et al. (2018b).

Halos and subhalos in each snapshot are identified using friends-of-friends (Davis et al. 1985) and SUBFIND (Springel et al. 2001) algorithms. To find the main progenitor of each halo, we use the merger tree made by SUBLINK (Rodriguez-Gomez et al. 2015). In this paper, we refer to galaxy groups and clusters as "hosts" and the galaxies that have been accreted by these hosts as "satellites."

2.2. Sample Selection

For completeness of the galaxy samples, we select galaxies whose stellar mass ($M_{*,\mathrm{gal}}$) is more massive than $10^9\,M_\odot$, which corresponds to more than 100 star particles. The TNG300 includes 4824 groups ($10^{13}\,M_\odot \leqslant M_{\mathrm{host}} < 10^{14}\,M_\odot$) and 426 clusters ($M_{\mathrm{host}} \geqslant 10^{14}\,M_\odot$), where M_{host} is the virial mass of each host at $z = 0$. The total number of satellites selected as the galaxy samples for the groups and clusters is 40,139 and 25,535, respectively.

We use the SFR and star-forming main sequence (MS) to divide galaxies into star-forming and quenched galaxies; i.e., the log SFR of quenched galaxies is 1 dex below the star-forming MS (Donnari et al. 2019). In this study, the SFR of the galaxies is calculated by stars that have formed in the last 200 Myr (Donnari et al. 2019; Pillepich et al. 2019). The star-forming MS is calculated by the following procedure (Donnari et al. 2019; Pillepich et al. 2019): (1) we calculate the median SFR of the star-forming galaxies in 0.2 dex logarithmic bins in the range of $M_{*,\mathrm{gal}} = 10^9$–$10^{10.2}\,M_\odot$, performing a fit to the median SFR linearly; (2) we recalculate the new median SFR excluding quenched galaxies, whose SFR is 1 dex below the previous median SFR; and (3) we repeat the second step until the median SFR converges to a given accuracy (1%). Finally, we linearly extrapolate the SFR to calculate the median SFR of star-forming galaxies more massive than $M_{*,\mathrm{gal}} > 10^{10.2}\,M_\odot$. The slope and y-intercept used in the linear fitting are 0.77 and -7.77, respectively.

The left panel of Figure 1 shows the SFR of all galaxies in TNG300 with $M_{*,\mathrm{gal}}$ at $z = 0$. The criterion between star-forming and quenched galaxies is shown as the black solid line, which is 1 dex below the star-forming MS (black dashed line). The right panel of Figure 1 shows the fraction of quenched galaxies out of all galaxies in individual hosts (f_{Q}, hereafter "the quenched fraction") at $z = 0$ as a function of M_{host}. In this panel, the mean $f_{\mathrm{Q}}(z = 0)$ increases with M_{host}, and the scatter

[5] http://www.tng-project.org

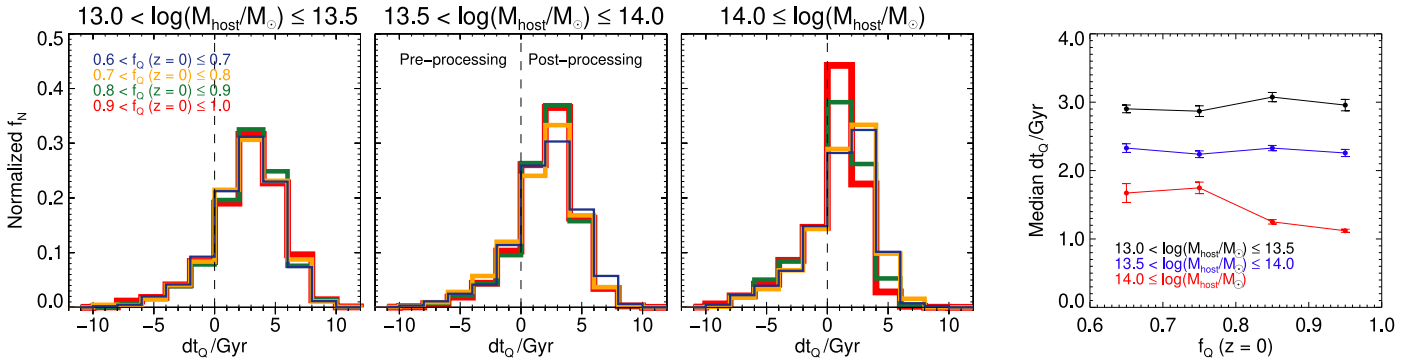

Figure 2. Left: normalized number of satellites with the time interval (dt_Q) from when they first fall into the host until they are quenched. In each M_{host} bin, we divide the satellites according to $f_Q(z=0)$ ranging from 0.6 to 1.0 with a 0.1 interval (blue, orange, green, and red lines). The gray dashed lines are the infall times of the satellites. Right: median dt_Q of satellites with $f_Q(z=0)$ in each M_{host} bin. Error bars indicate the standard error.

in $f_Q(z=0)$ decreases as M_{host} increases (e.g., Donnari et al. 2021a, 2021b). To check whether this trend is an intrinsic or a statistical scatter, we resample the hosts with a bootstrapping resampling in each mass bin while each mass bin has an equal number of hosts. We can still see the increasing scatter with decreasing M_{host}, so this trend is an intrinsic scatter, not a statistical scatter, from the poor number of high-mass hosts. The results are consistent even if the quenched galaxies are replaced with red galaxies (see the Appendix).

Note that various papers have shown that the effective kinetic AGN feedback mode quenches most galaxies with $M_{*,gal} > 10^{10.3}\ M_\odot$ (e.g., Nelson et al. 2018; Terrazas et al. 2020; Donnari et al. 2021b). In our sample, galaxies more massive than $10^{10.3}\ M_\odot$ are mostly quenched by strong AGN feedback. To check how AGN feedback affects the results in Figure 1, we examine the relation between $f_Q(z=0)$ and M_{host} using low-mass satellites ($M_{*,gal} < 10^{10.3}\ M_\odot$). Although there is an offset of the median $f_Q(z=0)$ of the low-mass satellites (~0.1 dex lower than that of all satellites), we find that the trend of the median $f_Q(z=0)$ of low-mass satellites is similar to that of all satellites: (1) $f_Q(z=0)$ is increasing with M_{host}, and (2) the size of the error bars is decreasing with M_{host}.

3. Host-mass Dependency and the Scatter of Quenched Fractions

We investigate why the mean $f_Q(z=0)$ increases with M_{host} by dividing the hosts into three mass ranges: low-mass ($10^{13.0}\ M_\odot < M_{host} \leqslant 10^{13.5}\ M_\odot$), intermediate-mass ($10^{13.5}\ M_\odot < M_{host} \leqslant 10^{14.0}\ M_\odot$), and high-mass ($10^{14.0}\ M_\odot \leqslant M_{host}$) bins or hosts. We then examine the origin of a scatter in $f_Q(z=0)$.

3.1. The Effects of Pre- and Post-processing on the Quenched Fraction

In the right panel of Figure 1, the mean $f_Q(z=0)$ is increasing with M_{host}: a host-mass dependency of $f_Q(z=0)$, shown in various observations (e.g., Muzzin et al. 2013; Fang et al. 2018; Jian et al. 2018; Donnari et al. 2021a; Reeves et al. 2023). To investigate the origin of the host-mass dependency of $f_Q(z=0)$, we measure the time interval (dt_Q) of each satellite from when it first falls into the host until it is quenched. Quenched satellites are defined by the MS at each snapshot, and we define the time of quenching/infall as the time of the first snapshot when galaxies are identified as quenched/satellites.

The left three panels of Figure 2 show the normalized number of galaxies (f_N) with dt_Q for hosts in three different mass bins. Here the negative dt_Q indicates that the satellites have been quenched before infall, while the positive dt_Q indicates quenching after infall. Regardless of M_{host}, the number of satellites that are quenched after falling into their final hosts is dominant ($dt_Q > 0$); the number fraction of quenched galaxies after infall is 0.84, 0.81, and 0.70 for low-, intermediate-, and high-mass bins, respectively. This means that pre-processing may have contributed to reducing the SF but not fully quenched satellites, but post-processing mainly contributes to the galaxy quenching (e.g., Donnari et al. 2021b). The decreasing number fraction of quenched fractions after infall for more massive hosts indicates that there are more pre-processed satellites in the more massive hosts (e.g., Hou et al. 2014; van der Burg et al. 2018; Bahé et al. 2019). Because satellites in more massive hosts can have more massive infalling groups than less massive hosts (e.g., Hou et al. 2014; van der Burg et al. 2018; Sarron et al. 2019; Donnari et al. 2021a), they are more likely to be quenched than those in low-mass hosts (e.g., Reeves et al. 2023; Salerno et al. 2022). Indeed, among the total number of quenched satellites, 25.8% of those in low-mass hosts and 50.2% of those in high-mass hosts are members of other structures when they fall into the final low- and high-mass hosts (e.g., Han et al. 2018; Donnari et al. 2021a).

Note that these results can be affected by the high-mass satellites that experience strong AGN feedback. When we measure the normalized f_N of low-mass satellites ($M_{*,sat} < 10^{10.3}\ M_\odot$), most of them are quenched by post-processing, not pre-processing. This means that most pre-processed satellites are quenched by strong AGN feedback in our sample (e.g., Donnari et al. 2021b). However, the results in Figure 2 are still shown when we only consider the low-mass satellites: (1) the number of post-processed low-mass satellites is more than that of pre-processed low-mass satellites, and (2) the median dt_Q of low-mass satellites decreases with increasing M_{host}.

The other thing that we have to notice in the left three panels of Figure 2 is that the peak dt_Q is getting shorter as M_{host} is increasing. To measure this trend quantitatively, we plot the median dt_Q with $f_Q(z=0)$ (right panel of Figure 2). In high-mass hosts, which generally have denser and more extended gas reservoirs (intracluster/intergalactic medium), ram pressure stripping is more efficient and affects infalling satellites earlier, making the satellites quench faster compared to those in low-

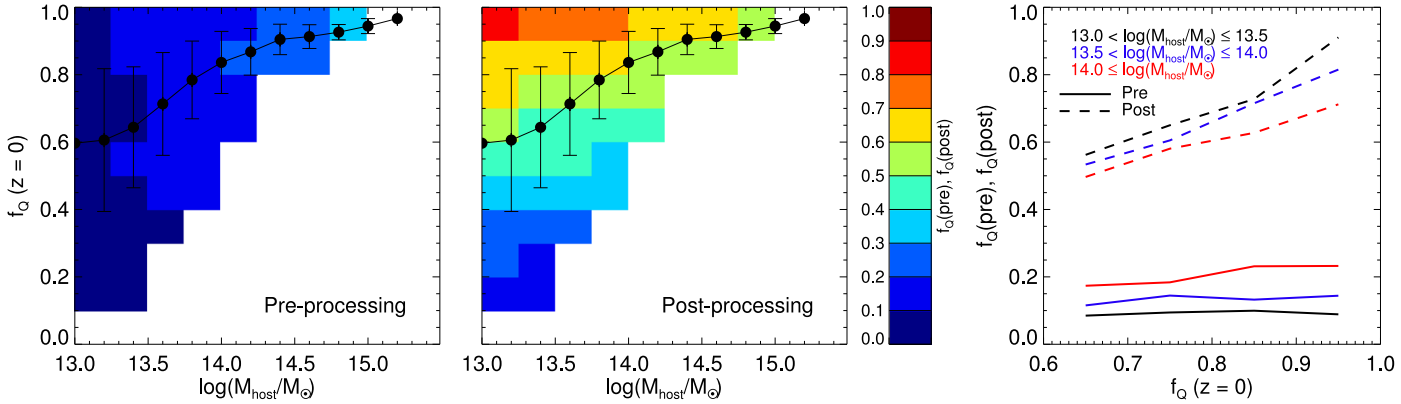

Figure 3. Left: 2D histograms showing the distribution of the mean $f_Q(z=0)$ and $M_{\rm host}$. The color indicates the mean f_Q(pre) of the satellites in each pixel before they fall into their hosts. Black dots with 1σ error bars are the same as in the right panel of Figure 1. Middle: same as the left panel, but the color denotes f_Q(post). Right: f_Q(pre) and f_Q(post) as a function of $f_Q(z=0)$ in each mass bin.

mass hosts (e.g., Jaffé et al. 2015; Boselli et al. 2016). As a result, satellites in high-mass hosts undergo more intense pre- and post-processing than those in low-mass hosts. This enables high-mass hosts to have higher $f_Q(z=0)$ than low-mass hosts, as shown in the right panel of Figure 1.

Interestingly, the median dt_Q is steeply decreasing with $f_Q(z=0)$ in a high-$M_{\rm host}$ bin (red line in the right panel of Figure 2). This trend is coming from the fact that the high-mass bin covers a wide range of $M_{\rm host}$ from $10^{14}\,M_\odot$ up to $\sim 10^{15.5}\,M_\odot$. Indeed, among high-mass hosts, hosts with $0.8 < f_Q(z=0) \leqslant 1.0$ are more massive than other hosts with $0.6 < f_Q(z=0) \leqslant 0.8$, on average. Because more massive hosts might experience the most efficient pre- and post-processing, satellites in more massive hosts are more rapidly quenched than those in less massive hosts.

In Figure 2, we demonstrate why high-mass hosts have higher $f_Q(z=0)$ than low-mass hosts; satellites in high-mass hosts experience pre-processing most strongly (0.30; low- and intermediate-mass hosts are 0.16 and 0.19, respectively) and are rapidly quenched by efficient post-processing. However, Figure 2 does not clearly show whether pre- or post-processing contributes to the scatter of $f_Q(z=0)$ as shown in the right panel of Figure 1. To investigate this, we separately examine the fraction of pre- and post-processing and plot the left two panels in Figure 3, which shows the effects of f_Q(pre) and f_Q(post) on $f_Q(z=0)$. The fractions of f_Q(pre) and f_Q(post) are calculated by taking an average of the number of pre- and post-processed satellites in each host. For the statistical significance, we use bins that have more than 10 data. In the left panel of Figure 3, the mean f_Q(pre) depends on $M_{\rm host}$ but not $f_Q(z=0)$, so only the host-mass dependency of f_Q(pre) is shown (see also Figure 2). This demonstrates that satellites are slightly quenched by pre-processing that depends on $M_{\rm host}$ before they fall into their final hosts. However, in the middle panel of Figure 3, the mean f_Q(post) depends not only on $M_{\rm host}$ but also $f_Q(z=0)$, which demonstrates that post-processing makes most satellites quenched and the large scatter in $f_Q(z=0)$ of low-mass hosts.

To measure the number of pre- and post-processed satellites quantitatively, we plot f_Q(pre) and f_Q(post) as a function of $f_Q(z=0)$ in the right panel of Figure 3. We take an average of f_Q(pre) and f_Q(post) in each $f_Q(z=0)$ bin so that $f_Q(z=0) = f_Q$(pre) + f_Q(post). Satellites in high-mass hosts have a slightly higher f_Q(pre) than those in low- and intermediate-mass hosts, indicating that pre-processing is more effective for them (e.g., Donnari et al. 2021b). However, f_Q(pre) is almost constant with $f_Q(z=0)$ at $M_{\rm host}$, which means that pre-processing strongly depends on $M_{\rm host}$, not $f_Q(z=0)$. On the other hand, f_Q(post) increases with decreasing $M_{\rm host}$ because satellites in low-mass hosts are less quenched by pre-processing than those in intermediate- and high-mass hosts. In addition, the mean $f_Q(z=0)$ at a fixed $M_{\rm host}$ strongly depends on f_Q(post). Therefore, although satellites are slightly quenched by pre-processing that depends on $M_{\rm host}$, post-processing that makes most satellites quenched mainly causes the scatter of $f_Q(z=0)$.

3.2. The Effect of the Infall Time of Satellites on the Quenched Fraction

In Figure 3, we show that post-processing makes the scatter of $f_Q(z=0)$; there is a diversity of $f_Q(z=0)$ values in a narrow range of $M_{\rm host}$. In this section, we focus on the factors that drive the diversity $f_Q(z=0)$ values. As shown in Figures 2 and 3, post-processing plays an important role in galaxy quenching, so the time when satellites fall into their hosts and how long they stay in their hosts can have a significant impact on galaxy quenching (e.g., Smith et al. 2019). To investigate this further, we define the infall time ($T_{\rm IF}$) as the time when satellites first fall into their final hosts and measure it as a look-back time. A large median $T_{\rm IF}$ in a given $M_{\rm host}$ bin indicates that the hosts gain their satellites early, while a small median $T_{\rm IF}$ represents hosts that gained their satellites recently. Thus, the median $T_{\rm IF}$ indicates the mass growth history of hosts within a similar range of $M_{\rm host}$.

The left three panels of Figure 4 show the cumulative fraction of satellites with $T_{\rm IF}$, indicating that satellites in hosts with high $f_Q(z=0)$ fall into their hosts early, regardless of $M_{\rm host}$. These early-infall satellites stay in their hosts long enough so that most of these satellites are quenched by post-processing. To measure this trend quantitatively, we plot the median $T_{\rm IF}$ with $f_Q(z=0)$ in the right panel of Figure 4. The median $T_{\rm IF}$ increases with $f_Q(z=0)$, supporting the result that a large number of satellites that fall into their hosts early are more likely to be quenched by post-processing. In other words, satellites have a high probability of being quenched as they stay longer in their hosts. Furthermore, at a fixed median $T_{\rm IF}$, high-mass hosts have the highest $f_Q(z=0)$ because satellites in high-mass hosts experience pre-processing most strongly and are rapidly quenched by post-processing (as shown in Section 3.1).

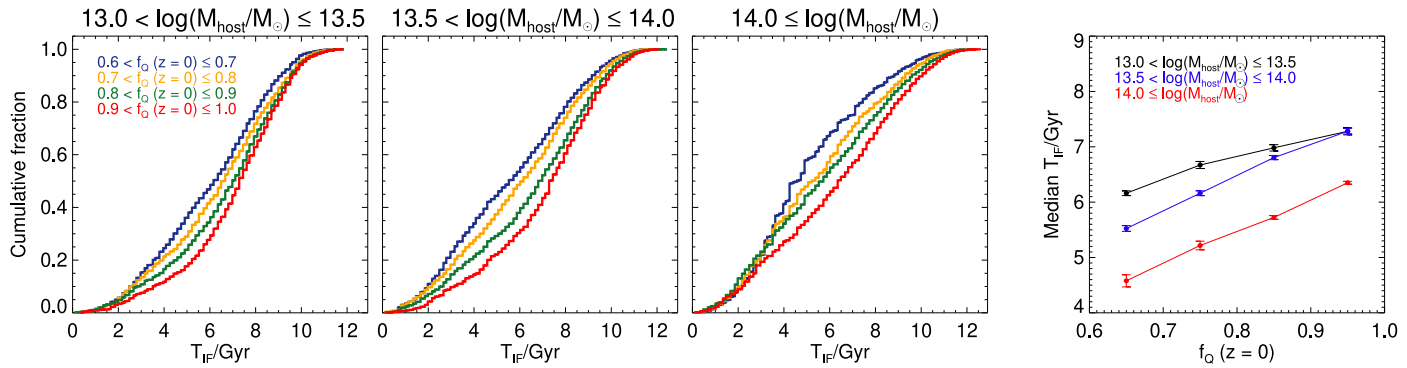

Figure 4. Left: cumulative fraction of satellites as a function of the infall time ($T_{\rm IF}$) when the satellites fall into their hosts. Right: median $T_{\rm IF}$ as a function of $f_{\rm Q}(z=0)$ in each mass bin with an error bar indicating the standard error.

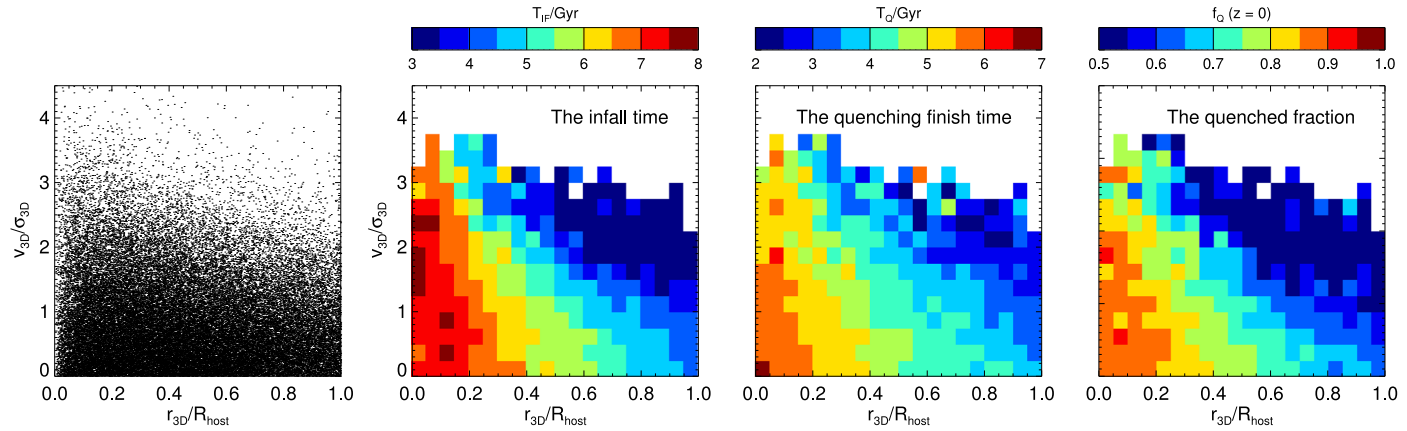

Figure 5. Distributions in the 3D phase-space diagram of the satellites (first panel), where $R_{\rm host}$ is a viral radius of the hosts. In the 3D phase-space diagram for the satellites, the colors indicate the mean $T_{\rm IF}$ (second panel), quenching finish time ($T_{\rm Q}$; third panel), and $f_{\rm Q}(z=0)$ (fourth panel) in each pixel of the grid.

The early-infall satellites lose their orbital energy due to the gravitational drag force and gradually move toward the center of the hosts, known as "dynamical friction" (Chandrasekhar 1943). As a result, early-infall satellites tend to stay close to the center of their hosts, losing their orbital energy, while late-infall satellites are more likely to be located in the outskirts of their hosts. This spatial separation between early- and late-infall satellites is shown in a phase-space diagram, which is a useful tool for studying the relationship between the infall time of satellites and their location in hosts (e.g., Oman & Hudson 2016; Rhee et al. 2017; Reeves et al. 2023). To investigate how the $T_{\rm IF}$ and $f_{\rm Q}(z=0)$ of satellites are shown in a phase-space diagram, we plot the left panel of Figure 5. Satellites that fall into their final hosts early are located in the innermost region, indicating that these satellites might have spent most of their time in their final hosts. We also plot the quenching finish time ($T_{\rm Q}$) of satellites in a phase-space diagram to compare it with $T_{\rm IF}$. We define $T_{\rm Q}$ as $T_{\rm IF} - dt_{\rm Q}$, which represents the look-back time when the quenching of satellites is completed. The similarity in color gradient between $T_{\rm IF}$ and $T_{\rm Q}$ indicates that satellites that fall into their hosts earlier tend to be quenched earlier by post-processing (e.g., Smith et al. 2019). Finally, we plot the right panels of Figure 5 to examine the relationship of $T_{\rm IF}$ and $T_{\rm Q}$ to $f_{\rm Q}(z=0)$. This shows that the satellites located in the innermost region are the most quenched. The good agreement in color gradient of the three right panels in Figure 5 shows that satellites that fall into their final hosts early could be the most quenched because they have enough time in their hosts.

In Figure 4, we show that hosts with a higher $f_{\rm Q}(z=0)$ have a higher median $T_{\rm IF}$ than those with a lower $f_{\rm Q}(z=0)$. To compare this result with the observation, we can use an observable projected phase-space diagram that can estimate the mean $T_{\rm IF}$ (H. Jeong et al. 2023, in preparation). Based on the results in Figure 5, the satellites can be divided into early- and late-infall satellites in a projected phase-space diagram (see also Oman & Hudson 2016; Rhee et al. 2017). To define early- and late-infall satellites, we measure the projected radius ($r_{\rm proj}$) and the line-of-sight velocity ($v_{\rm LOS}$) of each satellite. For the projected radius, we take an average of the radius from the center of the hosts to their satellites in each x–y, y–z, and x–z plane. For the line-of-sight velocity, we correct the Hubble flow (Oman & Hudson 2016, see their Equation (2)) and take an average of $v_{\rm LOS}$ in each x–y, y–z, and x–z plane. The left panel of Figure 6 shows early- and late-infall satellites defined as "ancient infallers" (A) and "recent infallers" (R; e.g., Rhee et al. 2017; Jeong et al. 2019).[6] We define region A, which includes most ancient infallers that fall into their final hosts before 6.45 Gyr, and region R, which includes most first infallers that have not yet fallen into their final hosts but will (see Table 2 and Figure 6 of Rhee et al. 2017).

The middle panel of Figure 6 shows the fraction of ancient infallers, $f_{\rm ancient} = A/(A+R)$, with $f_{\rm Q}(z=0)$. As $f_{\rm Q}(z=0)$ increases, $f_{\rm ancient}$ also increases, which indicates that hosts with high $f_{\rm Q}(z=0)$ have many ancient infallers, so the hosts

[6] Note that we follow the method of Jeong et al. (2019), who divided the phase-space diagram into two regions for statistical significance, unlike Rhee et al. (2017), who divided it into five regions.

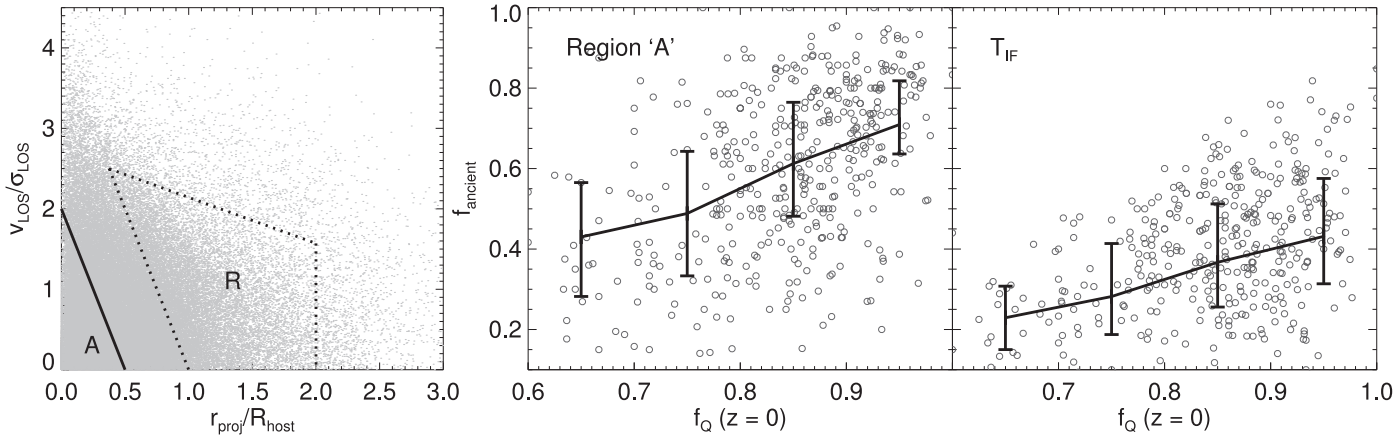

Figure 6. Left: regions on the projected phase-space diagram that we use to calculate $f_{\rm ancient}$ (see text for details), where gray dots are the distribution of satellites. Middle: relation between $f_{\rm Q}(z=0)$ and $f_{\rm ancient}$ of hosts more massive than $M_{\rm host} \geqslant 10^{14}\,M_{\odot}$. Ancient infallers are defined as satellites in region A. The black solid line connects the median values, and the error bars show the first and third quartiles. Right: symbols are the same as in the middle panel, but ancient infallers are defined as satellites that fell into their hosts 6.45 Gyr ago.

gain their mass early. Thus, ancient infallers are likely to be more quenched by post-processing because they have spent most of their time in their final hosts.

Since we define ancient infallers as satellites within region A, which is determined by projected position and velocity, the projection effect may cause some nonmember satellites to be included in region A. To check the projection effect of the observation in the middle panel, we alternatively define "ancient infallers" as satellites that fell into their hosts 6.45 Gyr ago (Rhee et al. 2017, see their Table 2) using $T_{\rm IF}$ instead of region A. The right panel of Figure 6 shows the results. When we use $T_{\rm IF}$, which can be measured in simulations, the value of $f_{\rm ancient}$ is much smaller than the value in the middle panel because, among the ancient infallers in the middle panel, about 30% of them fall into their hosts after 6.45 Gyr. This implies that a large number of recent infallers are misidentified as ancient infallers due to projection effects. However, both panels show that hosts with high $f_{\rm Q}(z=0)$ tend to have a large population of ancient infallers, which suggests that they have grown earlier compared to hosts with low $f_{\rm Q}(z=0)$. The trend of $f_{\rm ancient}$ that is measured from a phase-space diagram (middle panel) is similar to what is measured from $T_{\rm IF}$ in simulations (right panel). Thus, we can estimate the mass growth of hosts from the observable value of $f_{\rm ancient}$.

Note that high-mass galaxies ($10^{10.5}\,M_{\odot} < M_{*,\rm gal} < 10^{11.0}\,M_{\odot}$) in IllustrisTNG are overquenched by strong baryonic feedback from AGN (Nelson et al. 2018). Overquenching makes quenched fractions high compared to observations (e.g., Sherman et al. 2020; Angthopo et al. 2021), so there might be some offset of $f_{\rm Q}(z=0)$ between simulations and observations. However, we can still compare hosts with more early growth to those with more recent growth by using the relative values of $f_{\rm Q}(z=0)$.

4. Quenched Fractions with Various Properties of Hosts

In this section, we investigate various properties of the hosts that are related to their mass growth history and $f_{\rm Q}(z=0)$. There are various observational properties of galaxy clusters: the abundance of satellites, density, colors, morphology, ellipticity, isotropy, and so on. Among them, we use the abundance of satellites, ellipticity (ϵ), number density ($\rho_{\rm n}$), nearest distance to groups or clusters ($D_{\rm G13}$), and isotropy of satellites (β). Satellites whose stellar mass ($M_{*,\rm sat}$) is larger than $10^9\,M_{\odot}$ are used to calculate each property. The cluster formation time ($z_{\rm m50}$), which is the redshift when hosts first reach 50% of $M_{\rm host}(z=0)$, is included as an indicator of the mass growth history of the hosts (e.g., Chun et al. 2023). Unlikely other observational properties, $z_{\rm m50}$ is not an observable property. However, we have already investigated the different $T_{\rm IF}$ that can affect the scatter of $f_{\rm Q}(z=0)$, so how $z_{\rm m50}$ can affect $f_{\rm Q}(z=0)$ has to be examined.

We define the abundance of satellites as

$$\frac{N_{\rm sat}}{M_{\rm host}} \times 10^{12}, \tag{1}$$

where $N_{\rm sat}$ is the number of satellites in the virial radius ($R_{\rm host}$). We use the abundance normalized by $M_{\rm host}$ because, in general, $N_{\rm sat}$ depends strongly on $M_{\rm host}$ (e.g., Wu et al. 2022; see their Figure 5, left panel). Thus, if the abundance is small in a given range of $M_{\rm host}$, the hosts are dynamically more evolved than hosts with a large abundance.

We calculate the total ellipticity (ϵ) using the positions of satellites relative to the hosts (Shin et al. 2018; see their Equations (5)–(8) for details). We measure the ellipticity of satellites in $R_{\rm host}$ in the x–y, y–z, and x–z planes and take an average of these ellipticities (ϵ). Thus, ϵ denotes how satellites inside the host distribute.

To measure the number density of satellites around each host ($\rho_{\rm n}$), we count the number of satellites from $R_{\rm host}$ to $3R_{\rm host}$. We calculate the nearest distance ($D_{\rm G13}$) to any group or cluster whose $M_{\rm host}$ is larger than $10^{13}\,M_{\odot}$. Thus, hosts with small $D_{\rm G13}$ are located in denser environments, while those with larger $D_{\rm G13}$ are in less dense regions.

We measure the isotropy of satellites from zero to $5R_{\rm host}$ using the azimuthal symmetric excess (β; Gouin et al. 2022) with harmonic orders of $m=1$–4,

$$\beta = \sum_{m=1}^{n} \beta_m = \sum_{m=1}^{n} \frac{|Q_m|}{|Q_0|}, \tag{2}$$

where $|Q_m|$ is the modulus of the aperture multipole moment at the order of m. In the x–y, y–z, and x–z planes, we compute β and take an average of these three β.

Figure 7 shows 2D histograms of $z_{\rm m50}$ and various observational properties of hosts with $M_{\rm host}$. The properties of the hosts and $M_{\rm host}$ are divided into 10 bins to examine their

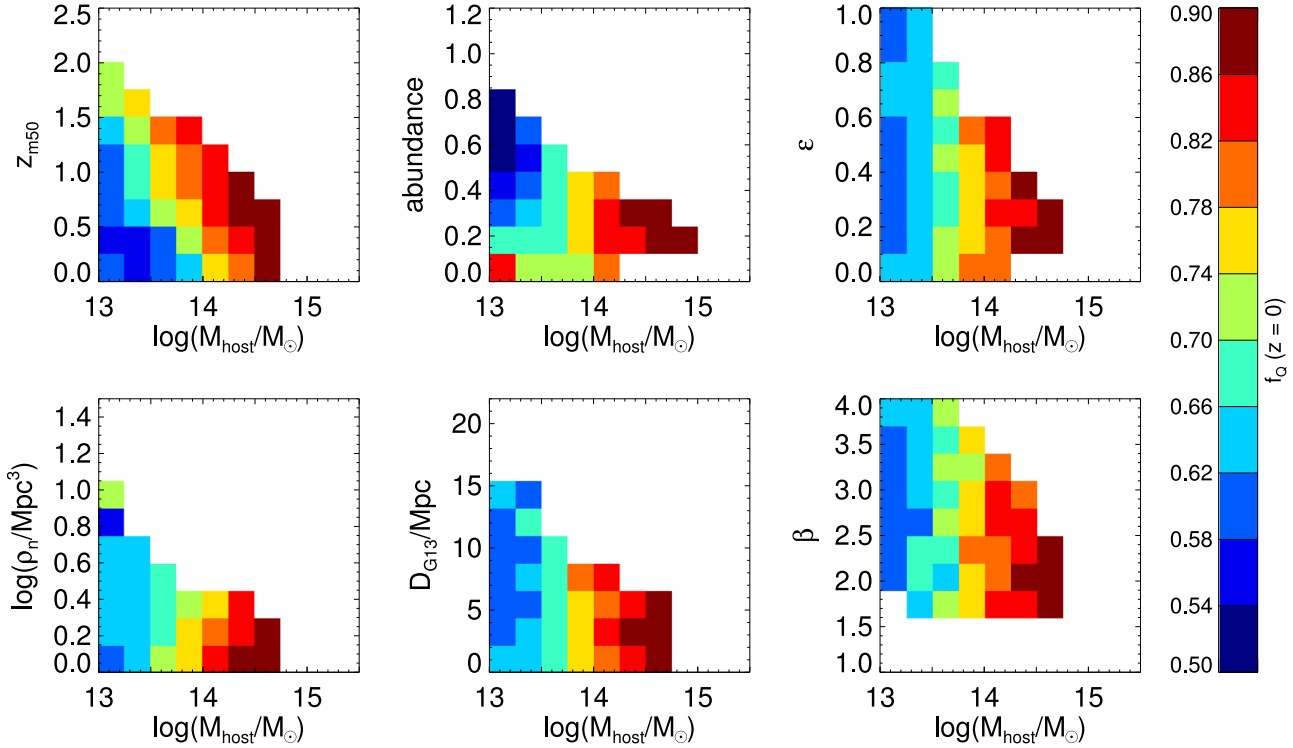

Figure 7. The 2D histograms of various properties of hosts with $M_{\rm host}$: the host formation time ($z_{\rm m50}$), abundance, ellipticity (ϵ), number density ($\rho_{\rm n}$), nearest distance to groups or clusters ($D_{\rm G13}$), and isotropy (β). Color scales are $f_{\rm Q}(z=0)$ at $z=0$. For statistical reliability, we use pixels that have more than 10 data points.

variations. We find that $f_{\rm Q}(z=0)$ strongly depends on $M_{\rm host}$ (vertical colored stripes) and weakly depends on $z_{\rm m50}$ (diagonal colored stripes) and the abundance of satellites (only when $M_{\rm host}$ is small). In Sections 3.1 and 3.2, we find that post-processing is more important for galaxy quenching than pre-processing; that is, satellites falling into their hosts early are likely to be more quenched due to a longer stay in their hosts compared to those falling later. Hosts with a high $z_{\rm m50}$ have many early-infall satellites (a high mean $T_{\rm IF}$), while those with a low $z_{\rm m50}$ have many late-infall satellites (a low mean $T_{\rm IF}$). Therefore, the different mass growth history results in diverse values of $f_{\rm Q}(z=0)$.

On the other hand, in low-mass hosts, $f_{\rm Q}(z=0)$ decreases with an increase in the abundance of satellites. In a given range of $M_{\rm host}$, hosts are dynamically unrelaxed if the abundance of satellites is high, indicating that satellites have fallen recently. These satellites have not stayed in their hosts long enough to be quenched, so eventually, the hosts could have low $f_{\rm Q}(z=0)$. Other properties of hosts, ϵ, ρ_n, $D_{\rm G13}$, and β, do not show the relation to $f_{\rm Q}(z=0)$ because those properties are related to the environment or mass distribution rather than the mass growth history of hosts.

To quantitatively measure the variation of $f_{\rm Q}(z=0)$ with the various properties of the hosts in Figure 7, we plot Figure 8. Only low-mass hosts ($10^{13}\,M_\odot < M_{\rm host} < 10^{13.5}\,M_\odot$) are used for statistical reliability. We first sort the values of each property in ascending order and then divide each property into five ranks of 0%–20%, 20%–40%, 40%–60%, 60%–80%, and 80%–100%; i.e., rank 1 represents the lowest value of each property, and rank 5 denotes the highest value. Next, we calculate the mean $f_{\rm Q}(z=0)$ of each rank. In Figure 8, the mean $f_{\rm Q}(z=0)$ decreases with the abundance of satellites and increases with $z_{\rm m50}$. Hosts with a high $z_{\rm m50}$ gain their mass early due to the early infall of their satellites. Early-infall

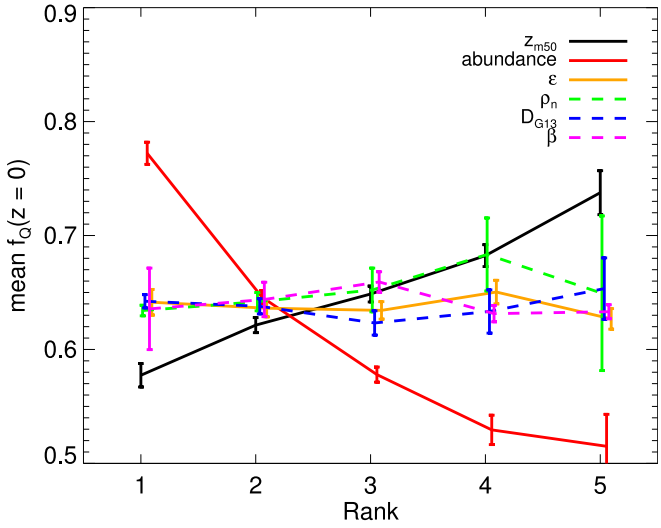

Figure 8. Relation between $f_{\rm Q}(z=0)$ and the rank of various properties of hosts (see text for details). The data in Figure 7 are used to calculate ranks.

satellites have spent more time in the potential of their hosts, on average, and naturally lose more mass as they are subjected to post-processing, which can affect not only the mass loss but also the destruction of satellites. For example, after satellites fall into their hosts, they experience hydrodynamical interaction with the intracluster medium (ICM; e.g., Gunn & Gott 1972), ram pressure stripping, so satellites can halt the SF activity. Satellites are also affected by gravitational tides in the potential well of their hosts, so DM, stars, and gas in satellites can be stripped (e.g., Merritt 1984). Harassment (e.g., Moore et al. 1996) and galaxy mergers (e.g., Toomre & Toomre 1972) also can distort and destroy satellites. Some satellites lose their

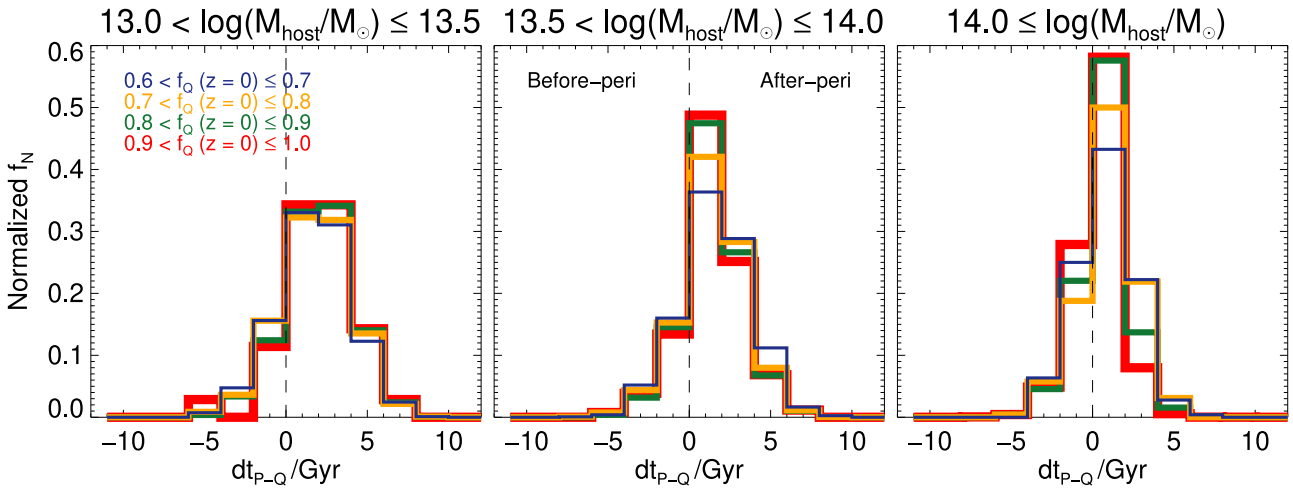

Figure 9. Normalized number of satellites with the time interval (dt_{P-Q}) from the time when the satellites pass by the pericenter to the quenching finish time in different M_{host} bins. In each mass bin, we divide the satellites according to $f_Q(z=0)$ ranging from 0.6 to 1.0 with a 0.1 interval (blue, orange, green, and red lines). The gray dashed lines denote the time when the satellites are passing by the pericenter.

orbital energy and finally merge into the cluster galaxy (brightest cluster galaxy) via dynamical friction (Chandrasekhar 1943). As a result, the destruction rate of early-infall satellites is higher, making the abundance of satellites lower. Therefore, in a low-M_{host} bin, the abundance of satellites and the fraction of quenched satellites at $z=0$ can be observable indicators of the mass growth history of hosts.

We find that in intermediate- and high-mass hosts, only z_{m50} has a relation to $f_Q(z=0)$. The dependence of T_{IF} with f_Q has already been shown (right panel of Figure 4), so we can still find this trend when it comes to z_{m50}. Satellites in intermediate- and high-mass hosts fell into their hosts more recently and are quenched more rapidly than those in low-mass hosts (right panels of Figures 2 and 4). However, these satellites are not disrupted easily, although they fell into their hosts a long time ago (e.g., Bahé et al. 2019). This makes the dependence of the abundance on f_Q weak unlikely in the case of low-mass hosts. Therefore, only the fraction of quenched satellites at $z=0$ can be used as an indicator of the mass growth history of intermediate- and high-mass hosts.

5. Effect of Host Pericenter Passage on Quenched Satellites

In this paper, we emphasize the importance of post-processing for satellites to be quenched because (1) most satellites are quenched after they fall into their final hosts, and (2) satellites that fall into their hosts are quenched by efficient post-processing, so the different mean T_{IF} of satellites makes a scatter of $f_Q(z=0)$. Although satellites can be quenched by some physical mechanisms, we are unable to differentiate between them. Instead, we can derive the effect of the passage of the pericenter for galaxy quenching. Various studies have shown that galaxies are quenched around the first pericenter (e.g., Rhee et al. 2020; Upadhyay et al. 2021). Upadhyay et al. (2021) analyzed a sample of 11 massive ellipticals in the Coma cluster. They found that SF in those ellipticals stops 1 Gyr after the first pericenter passage, and this rapid quenching comes from the combination of ram pressure stripping with tidal interactions. To investigate the effect of the passage of the pericenter of hosts on galaxy quenching, we trace the orbit of each satellite and measure the time interval from when satellites pass by the pericenter (T_{peri}) to the quenching finish time: $dt_{P-Q} = T_{peri} - T_Q$.

Figure 9 shows the normalized number of satellites with dt_{P-Q}. Note that we exclude satellites that are pre-processed or do not pass by the pericenter to see the effect of the pericenter. Satellites with $dt_{P-Q} > 0$ are quenched after passing by the pericenter, while those with $dt_{P-Q} < 0$ are quenched before. Most satellites are quenched after passing by the pericenter, so the interaction between the passage of the pericenter and the satellites is important for galaxy quenching. We find that high-mass hosts have a slightly higher quenched fraction before the pericenter (0.31) compared to low- and intermediate-mass hosts (0.21 and 0.22, respectively). Although we remove satellites that do not pass by the pericenter or stop SF by pre-processing, some satellites in high-mass hosts might have low SFRs, possibly approaching zero. This is because when these satellites fall into their high-mass hosts, they already have experienced efficient pre-processing (see Section 3.1) and post-processing, before the passage of the pericenter. This is why high-mass hosts have large quenched fractions before the passage of the pericenter. The mean dt_{P-Q} is 1.9, 1.4, and 0.6 Gyr in the low-, intermediate-, and high-mass bin, respectively. The shortest mean dt_{P-Q} in high-mass hosts might result from the efficient ram pressure stripping (e.g., Boselli et al. 2016; Oman & Hudson 2016) and tidal stripping (e.g., Upadhyay et al. 2021).

We also measure dt_{P-Q} with $M_{*,sat}$ to investigate how satellites are affected by the passage of the pericenter. Because high-mass satellites ($10^{10.3}\,M_\odot < M_{*,sat}$) are affected by strong AGN feedback, we only investigate the dt_{P-Q} of low-mass satellites ($10^{9.5} \leqslant M_{*,sat} < 10^{10.3}$). In the case of low-mass satellites, the average dt_Q and dt_{P-Q} are $\sim$3.1 and $\sim$1.4 Gyr, respectively, so low-mass satellites pass by the pericenter of their hosts after $\sim$1.7 Gyr since infall. This suggests that the SFR of low-mass satellites is rarely affected after the first infall, or the SFR is gradually suppressed via ram pressure stripping or strangulation (e.g., Wetzel et al. 2013; Taranu et al. 2014; Haines et al. 2015; Foltz et al. 2018; Maier et al. 2019; Roberts et al. 2019; Rhee et al. 2020). When low-mass satellites fall into their final hosts, the density of the ICM around the outskirts of the hosts is low, so cold gas in the satellites cannot interact with the ICM around them. During this phase, steady

gas depletion (starvation/strangulation) occurs in low-mass satellites. Thus, they can continue to increase their $M_{*,\mathrm{sat}}$ because their SFR is not completely suppressed. When satellites approach the inner region of their hosts, they can reach the threshold ICM density ($\sim 10^{-28}$ g cm^{-3}), and then a significant fraction of cold gas becomes susceptible to ram pressure stripping. Finally, satellites can be quenched after the passage of the pericenter of their hosts (e.g., Wetzel et al. 2013; Roberts et al. 2019; Rhee et al. 2020). The other thing that we have to pay attention to is that the $dt_{\mathrm{P-Q}}$ of low-mass satellites is increasing with $M_{*,\mathrm{sat}}$. If $M_{*,\mathrm{sat}}$ decreases, the potential well is getting shallower, so gases in low-mass satellites are likely to be stripped by tides or ram pressure (Jung et al. 2018; Rohr et al. 2023).

In this section, we investigate how the passage of the pericenter can affect the SF of satellites. We find that satellites in high-mass hosts are slightly more quenched than those in low- and intermediate-mass hosts due to efficient pre- and post-processing. After passing by the pericenter of high-mass hosts, satellites are most rapidly quenched due to the efficient ram pressure stripping. Low-mass satellites are rapidly quenched, passing by the pericenter after a delay phase. The time from the passage of the pericenter to being quenched increases with the stellar mass of the satellites because gases in low-mass satellites might be easily stripped due to a shallow potential well.

6. Summary

We investigate the fraction of quenched satellites of hosts whose virial mass is larger than $10^{13}\,M_{\odot}$ at $z=0$ using TNG300 in the IllustrisTNG cosmological magnetohydrodynamical simulations. In the simulations, the fraction of quenched satellites depends on the virial mass of the hosts, and there is a scatter of quenched fractions at $z=0$. Throughout the paper, we examine which physical mechanisms cause these results and which properties of hosts are related to the fraction of quenched satellites. Below is a summary of our results.

1. Post-processing is important for satellites to be quenched because (1) most satellites are quenched after falling into their hosts and (2) the fraction of quenched satellites at $z=0$ is increasing with the fraction of quenched satellites after infall.
2. Satellites in high-mass hosts experience pre-processing more than those in low- and intermediate-mass hosts, and they are rapidly quenched by efficient post-processing after falling into their hosts. This makes satellites in high-mass hosts most quenched at $z=0$, so there is a host-mass dependency of the fraction of quenched satellites at $z=0$.
3. The different infall times of satellites make a scatter in the fraction of quenched satellites at $z=0$ in a given mass range of hosts. Satellites that fall into their hosts early have spent most of their time in their hosts, so they could be more quenched than those falling lately. Thus, hosts with a high fraction of quenched satellites at $z=0$ have many early-infall satellites, while hosts with low quenched fractions have many late-infall satellites.
4. In a phase-space diagram, satellites that fall into their hosts early are located in the innermost region of hosts. These satellites have spent most of their time in their hosts and are most quenched by post-processing. Thus, if hosts have a high fraction of quenched satellites at $z=0$, the fraction of early-infall satellites is high, which means hosts gain their mass early. This indicates that if we know the fraction of quenched satellites at $z=0$, we can estimate the mass growth history of the hosts.
5. Among the various properties of the hosts, z_{m50} and the abundance of satellites are related to the fraction of quenched satellites at $z=0$ in low-mass hosts ($10^{13}\,M_{\odot} < M_{\mathrm{host}} \leqslant 10^{13.5}\ M_{\odot}$). Thus, the abundance and fraction of quenched satellites at $z=0$ can be indicators of the history of hosts indirectly in low-mass hosts. In intermediate- and high-mass hosts, only z_{m50} is related to the fraction of quenched satellites at $z=0$.
6. Most satellites are quenched after passing by the pericenter of their hosts. The time interval from when satellites pass by the pericenter to the quenching finish time decreases with the mass of the hosts because of effective ram pressure and tidal stripping in massive hosts. Furthermore, low-mass satellites seem to experience a delay phase before quenching because most of them spend more than half of their time after infall in the passage of the pericenter and then are quenched after the passage of the pericenter.

Acknowledgments

This work was supported by the Korea Astronomy and Space Science Institute under the R&D program (project No. 2023-1-830-01) supervised by the Ministry of Science and ICT (MSIT). K.W.C. was supported by a National Research Foundation of Korea (NRF) grant funded by the Korea government (MSIT; grant No. 2021R1F1A1045622). H.J. acknowledges support from a National Research Foundation of Korea (NRF) grant funded by the Korea government (MSIT; grant No. NRF-2019R1F1A1041086). J.H.L. acknowledges support from a National Research Foundation of Korea (NRF) grant funded by the Korea government (MSIT; grant No. 2022R1A2C1004025). This research was partially supported by the Australian Research Council Centre of Excellence for All Sky Astrophysics in 3 Dimensions (ASTRO 3D) through project No. CE170100013. J. S. acknowledges support from a National Research Foundation of Korea (NRF) grant funded by the Korea government (MSIT; grant No. 2022M3K3A1093827). R.S. acknowledges partial support from FONDECYT through grant 1230441.

Appendix
Plots Using the Red Galaxy Fraction

The red galaxies in TNG300 are defined as galaxies that have a $g-r$ color larger than $(g-r) = 0.5 \log M_{*,\mathrm{gal}} + 0.1$ mag (Pulsoni et al. 2020; see their Equation (6)). Figure A1 shows the red galaxy fraction (f_{R}) with M_{host} at $z=0$. The trend of $f_{\mathrm{R}}(z=0)$ increases with M_{host}, similar to the trend in the right panel of Figure 1.

We plot the mean $f_{\mathrm{R}}(z=0)$ in a phase-space diagram (left panel of Figure A2). The trend of color gradient is similar to that in the right panel of Figure 5. After ancient infallers are defined as satellites located in region A (see the left panel of Figure 6), we plot the fraction of ancient infallers with $f_{\mathrm{R}}(z=0)$ in the right panel of Figure A2. The fraction of ancient infallers increases with $f_{\mathrm{R}}(z=0)$, indicating that satellites falling into their hosts early become red galaxies more than those falling recently.

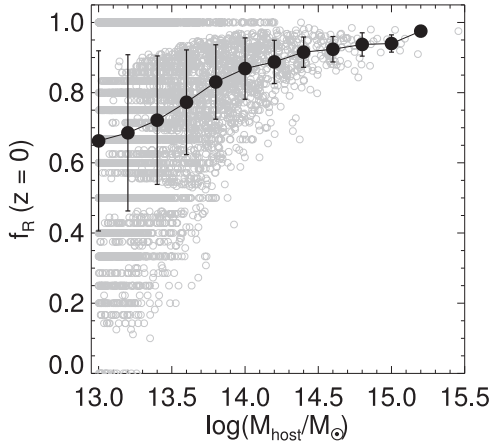

Figure A1. Number fraction of red galaxies (f_R) out of all galaxies in individual groups and clusters as a function of M_{host} at $z = 0$. Black dots are the mean f_R in each mass bin with 1σ errors.

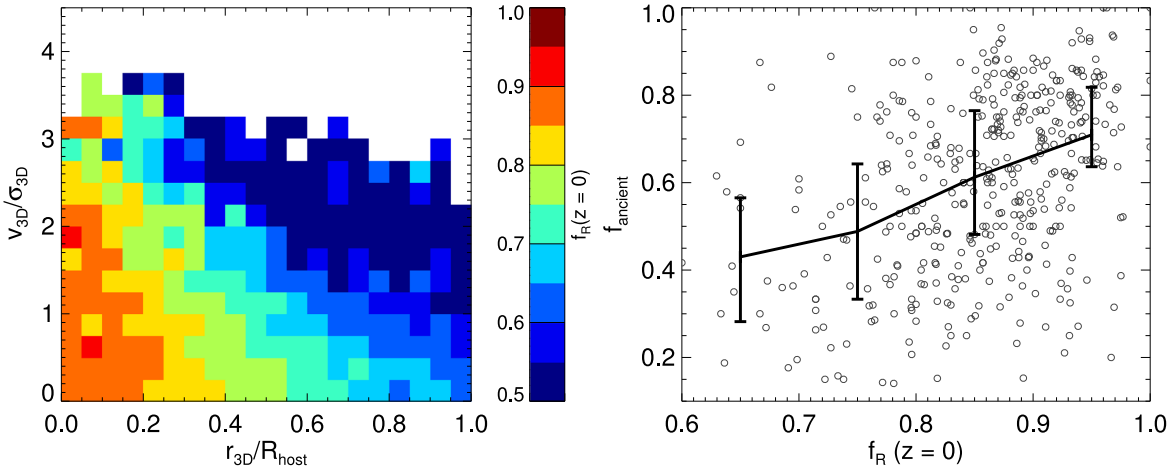

Figure A2. Left: mean $f_R(z = 0)$ in a phase-space diagram. Right: $f_{ancient}$ with $f_R(z = 0)$.

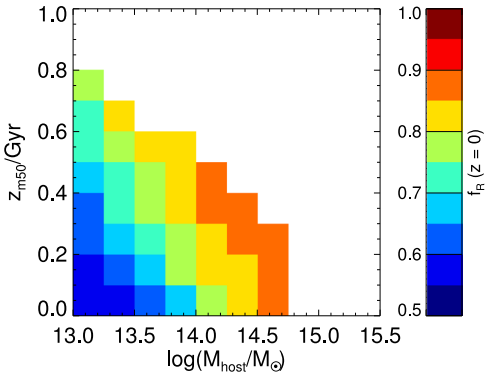

Figure A3. The 2D histogram of z_{m50} with M_{host}. The color bar represents $f_R(z = 0)$. Pixels that have more than 10 data are used for statistical reliability.

In Figure A3, we investigate the relation between z_{m50} and $f_R(z = 0)$. Similar to the upper left panel of Figure 7, $f_R(z = 0)$ can also be an indicator that represents the mass growth history of hosts.

ORCID iDs

So-Myoung Park https://orcid.org/0000-0003-1889-325X
Kyungwon Chun https://orcid.org/0000-0001-9544-7021
Jihye Shin https://orcid.org/0000-0001-5135-1693
Hyunjin Jeong https://orcid.org/0000-0002-0145-9556
Joon Hyeop Lee https://orcid.org/0000-0003-3451-0925
Mina Pak https://orcid.org/0000-0002-5896-0034
Rory Smith https://orcid.org/0000-0001-5303-6830
Jae-Woo Kim https://orcid.org/0000-0002-1710-4442

References

Angthopo, J., Negri, A., Ferreras, I., et al. 2021, MNRAS, 502, 3685
Bahé, Y. M., McCarthy, I. G., Balogh, M. L., & Font, A. S. 2013, MNRAS, 430, 3017
Bahé, Y. M., Schaye, J., Barnes, D. J., et al. 2019, MNRAS, 485, 2287
Balogh, M. L., Navarro, J. F., & Morris, S. L. 2000, ApJ, 540, 113
Boselli, A., Roehlly, Y., Fossati, M., et al. 2016, A&A, 596, A11
Brownson, S., Bluck, A. F. L., Maiolino, R., & Jones, G. C. 2022, MNRAS, 511, 1913
Chandrasekhar, S. 1943, ApJ, 97, 255
Chun, K., Shin, J., Smith, R., Ko, J., & Yoo, J. 2023, ApJ, 943, 148
Contini, E., Gu, Q., Ge, X., et al. 2020, ApJ, 889, 156
Cortese, L., Catinella, B., & Smith, R. 2021, PASA, 38, e035
Crossett, J. P., Pimbblet, K. A., Jones, D. H., Brown, M. J. I., & Stott, J. P. 2017, MNRAS, 464, 480
Davis, M., Efstathiou, G., Frenk, C. S., & White, S. D. M. 1985, ApJ, 292, 371
Di Matteo, T., Springel, V., & Hernquist, L. 2005, Natur, 433, 604
Donnari, M., Pillepich, A., Nelson, D., et al. 2019, MNRAS, 485, 4817
Donnari, M., Pillepich, A., Nelson, D., et al. 2021a, MNRAS, 506, 4760
Donnari, M., Pillepich, A., Joshi, G. D., et al. 2021b, MNRAS, 500, 4004
Fang, J. J., Faber, S. M., Koo, D. C., et al. 2018, ApJ, 858, 100
Fang, J. J., Faber, S. M., Koo, D. C., & Dekel, A. 2013, ApJ, 776, 63
Foltz, R., Wilson, G., Muzzin, A., et al. 2018, ApJ, 866, 136
Fujita, Y. 2004, PASJ, 56, 29

Gabor, J. M., Davé, R., Finlator, K., & Oppenheimer, B. D. 2010, MNRAS, 407, 749
Gallagher, John, S. I., & Ostriker, J. P. 1972, AJ, 77, 288
González Delgado, R. M., Rodríguez-Martín, J. E., Díaz-García, L. A., et al. 2022, A&A, 666, A84
Gouin, C., Gallo, S., & Aghanim, N. 2022, A&A, 664, A198
Gunn, J. E., Gott, J., & Richard, I. 1972, ApJ, 176, 1
Haines, C. P., Pereira, M. J., Smith, G. P., et al. 2015, ApJ, 806, 101
Han, S., Smith, R., Choi, H., et al. 2018, ApJ, 866, 78
Hou, A., Parker, L. C., & Harris, W. E. 2014, MNRAS, 442, 406
Jaffé, Y. L., Smith, R., Candlish, G. N., et al. 2015, MNRAS, 448, 1715
Jaffé, Y. L., Verheijen, M. A. W., Haines, C. P., et al. 2016, MNRAS, 461, 1202
Jeong, H., Kim, S., Owers, M. S., et al. 2019, ApJ, 875, 60
Jian, H.-Y., Lin, L., Oguri, M., et al. 2018, PASJ, 70, S23
Jung, S. L., Choi, H., Wong, O. I., et al. 2018, ApJ, 865, 156
Kauffmann, G., Heckman, T. M., White, S. D. M., et al. 2003, MNRAS, 341, 54
Larson, R. B., Tinsley, B. M., & Caldwell, C. N. 1980, ApJ, 237, 692
Li, P., Wang, H., Mo, H. J., Wang, E., & Hong, H. 2020, ApJ, 902, 75
Maier, C., Ziegler, B. L., Haines, C. P., & Smith, G. P. 2019, A&A, 621, A131
Man, A., & Belli, S. 2018, NatAs, 2, 695
Marinacci, F., Vogelsberger, M., Pakmor, R., et al. 2018, MNRAS, 480, 5113
Medling, A. M., Cortese, L., Croom, S. M., et al. 2018, MNRAS, 475, 5194
Merritt, D. 1984, ApJ, 276, 26
Mishra, Sapna, Muzahid, Sowgat, Dutta, Sayak, et al. 2023, arXiv:2305.05698
Moore, B., Katz, N., Lake, G., Dressler, A., & Oemler, A. 1996, Natur, 379, 613
Muzzin, A., Marchesini, D., Stefanon, M., et al. 2013, ApJ, 777, 18
Naiman, J. P., Pillepich, A., Springel, V., et al. 2018, MNRAS, 477, 1206
Nelson, D., Pillepich, A., Springel, V., et al. 2018, MNRAS, 475, 624
Nelson, D., Springel, V., Pillepich, A., et al. 2019, ComAC, 6, 2
Oman, K. A., & Hudson, M. J. 2016, MNRAS, 463, 3083
Peng, Y.-j., Lilly, S. J., Kovač, K., et al. 2010, ApJ, 721, 193
Peng, Y.-j., Lilly, S. J., Renzini, A., & Carollo, M. 2012, ApJ, 757, 4
Pillepich, A., Nelson, D., Hernquist, L., et al. 2018a, MNRAS, 475, 648
Pillepich, A., Nelson, D., Springel, V., et al. 2019, MNRAS, 490, 3196
Pillepich, A., Springel, V., Nelson, D., et al. 2018b, MNRAS, 473, 4077
Pulsoni, C., Gerhard, O., Arnaboldi, M., et al. 2020, A&A, 641, A60
Reeves, A. M. M., Hudson, M. J., & Oman, K. A. 2023, MNRAS, 522, 1779
Rhee, J., Smith, R., Choi, H., et al. 2017, ApJ, 843, 128
Rhee, J., Smith, R., Choi, H., et al. 2020, ApJS, 247, 45
Roberts, I. D., Parker, L. C., Brown, T., et al. 2019, ApJ, 873, 42
Rodriguez-Gomez, V., Genel, S., Vogelsberger, M., et al. 2015, MNRAS, 449, 49
Rohr, E., Pillepich, A., Nelson, D., et al. 2023, MNRAS, 524, 3502
Salerno, J. M., Muriel, H., Coenda, V., et al. 2022, MNRAS, 517, 4515
Sarron, F., Adami, C., Durret, F., & Laigle, C. 2019, A&A, 632, A49
Sarron, F., & Conselice, C. J. 2021, MNRAS, 506, 2136
Schaefer, A. L., Croom, S. M., Scott, N., et al. 2019, MNRAS, 483, 2851
Sherman, S., Jogee, S., Florez, J., et al. 2020, MNRAS, 499, 4239
Shin, T.-h., Clampitt, J., Jain, B., et al. 2018, MNRAS, 475, 2421
Smith, R., Pacifici, C., Pasquali, A., & Calderón-Castillo, P. 2019, ApJ, 876, 145
Springel, V., Pakmor, R., Pillepich, A., et al. 2018, MNRAS, 475, 676
Springel, V., White, S. D. M., Tormen, G., & Kauffmann, G. 2001, MNRAS, 328, 726
Taranu, D. S., Hudson, M. J., Balogh, M. L., et al. 2014, MNRAS, 440, 1934
Terrazas, B. A., Bell, E. F., Pillepich, A., et al. 2020, MNRAS, 493, 1888
Toomre, A., & Toomre, J. 1972, ApJ, 178, 623
Upadhyay, A. K., Oman, K. A., & Trager, S. C. 2021, A&A, 652, A16
van der Burg, R. F. J., McGee, S., Aussel, H., et al. 2018, A&A, 618, A140
Vijayaraghavan, R., & Ricker, P. M. 2013, MNRAS, 435, 2713
Wake, D. A., van Dokkum, P. G., & Franx, M. 2012, ApJL, 751, L44
Weinberger, R., Springel, V., Hernquist, L., et al. 2017, MNRAS, 465, 3291
Wetzel, A. R., Tinker, J. L., Conroy, C., & van den Bosch, F. C. 2013, MNRAS, 432, 336
Wu, J. F., Peek, J. E. G., Tollerud, E. J., et al. 2022, ApJ, 927, 121